Batteries & Supercaps

Review
doi.org/10.1002/batt.202400504

Chemistry Europe
European Chemical Societies Publishing

www.batteries-supercaps.org

Application of Noninvasive Imaging Techniques for High Energy Density Lithium Metal Rechargeable Batteries

Arghya Dutta*[a] and Shoichi Matsuda*[a, b, c]

Lithium metal batteries (LMBs) have the potential to exceed the energy density of current lithium-ion batteries. Achieving this requires a thick positive electrode, a thin Li metal negative electrode, and minimal electrolyte-loading. Despite their promise, high energy density LMBs with high-loading positive electrodes, thin Li, and low electrolytes face significant challenges. A key issue is the high reactivity of Li metal with nonaqueous electrolytes, leading to the consumption of both during each cycle. This reaction causes insulating Li compounds to accumulate, increases electrode porosity and thickness, depletes the electrolyte, raises cell impedance, and reduces capacity. Therefore, understanding the interphase evolution of the Li metal electrode is crucial to addressing cell failure. While various ex situ and in situ techniques have been used to study these interphases, they often involve non-practical cell configurations and sample-damaging preparation processes. In this regard, noninvasive methods like X-ray and neutron-based imaging are beneficial as they do not damage samples, can be used both in situ and ex situ, employ practical cell configurations, and enable long-term data collection. This review explores recent advancements in X-ray and neutron-based techniques for characterizing high-energy LMBs, emphasizing their potential to improve understanding of interphasial dynamics and advance robust high-energy-density batteries.

1. Introduction

In response to the escalating energy demands of modern society, it is essential to develop high-performance energy storage systems to achieve sustainable energy solutions.[1] For decades, rechargeable lithium-ion batteries (LIBs) have proven effective for powering portable electronic devices and have recently emerged as the primary technology for electric vehicles. Nonetheless, the need for batteries with greater energy density is growing to enable electric vehicles to travel longer distances at reduced costs.[2,3] A promising strategy to increase the energy density of LIBs is to substitute the graphite electrode, which has a theoretical specific capacity of 372 $mAh\,g^{-1}$, with a lithium metal (Li) electrode.[4] Li metal electrode provides an exceptional theoretical specific capacity of 3860 $mAh\,g^{-1}$, low redox potential (−3.04 V versus the standard hydrogen electrode), and low density (0.534 $g\,cm^{-3}$).

Despite the promise, the commercialization of lithium metal batteries (LMBs) faces significant challenges, primarily due to low Coulombic efficiency (CE) and the formation of needle-like Li dendrites, which can penetrate the separator and cause short circuits.[5–7] Although recent advancements in electrolyte formulations have significantly mitigated the dendrite issue, the low CE remains a critical concern due to the high reactivity of Li metal.[7–12] Typically, the surface of Li metal is coated with a native film, and upon contact with a nonaqueous electrolyte, a new layer called the solid electrolyte interphase (SEI) forms.[13,14] Ideally, this SEI layer should protect the Li metal surface from further reactions and stabilize the interphase. However, in practice, the SEI is mechanically unable to withstand the significant volume changes during Li plating and stripping cycles. Consequently, the SEI cracks, exposes fresh Li surfaces, and triggers continuous SEI formation.[15] This repeated SEI formation depletes active Li, resulting in lower CE and reduced cycle life. Additionally, the formation of electrically disconnected Li, or 'dead Li', also reduces the CE and cycle life.[16,17] The accumulation of insulating SEI compounds and 'dead Li', causing electrode volume expansion, increased electrode porosity, and entrapment of liquid electrolyte on the porous electrode surface, leads to increased cell impedance, voltage polarization, and premature cell failure.[18–21] Therefore, understanding the interphasial evolution of the Li metal electrode is crucial to addressing the interconnected problems of low CE, significant volume expansion, impedance growth, and short cycle life.

To investigate the interphasial processes on Li metal electrodes, both qualitatively and quantitatively, various analytical techniques have been applied. These include transmission electron microscopy (TEM), scanning electron microscopy (SEM), atomic force microscopy (AFM), optical microscopy (OM), X-ray photoelectron spectroscopy (XPS), and titration-

[a] A. Dutta, S. Matsuda
Center for Green Research on Energy and Environmental Materials, National Institute for Materials Science, 1–1 Namiki, Tsukuba, Ibaraki 305–0044, Japan
E-mail: DUTTA.arghya@nims.go.jp
MATSUDA.Shoichi@nims.go.jp

[b] S. Matsuda
NIMS-SoftBank Advanced Technologies Development Center, National Institute for Materials Science, 1–1 Namiki, Tsukuba, Ibaraki 305–0044, Japan

[c] S. Matsuda
Center for Advanced Battery Collaboration, National Institute for Materials Science, 1–1 Namiki, Tsukuba, Ibaraki 305–0044, Japan

based techniques etc.[22–35] Postmortem analyses using SEM and TEM offer high-resolution, site-specific insights into the interphasial morphologies of Li metal electrodes. However, the sample preparation required for these techniques often results in physical damage to the electrode surface, leading to potential inaccuracies. Furthermore, ex-situ methods cannot deliver time-resolved information. While in situ SEM and TEM studies can provide real-time visualization of electrode processes, they typically require cell configurations that differ significantly from actual batteries.[36–39] Additionally, the electron beams used in SEM and TEM can cause substantial damage to the sample under observation. In situ OM, although less invasive to the electrode surface structures, lacks sufficient spatial resolution.[24,40,41] Moreover, the cell configuration used for in situ OM, which often involves large quantities of electrolyte and physically separated electrodes without stack pressure, does not represent practical battery cells. Moreover, the microscopic techniques fail to provide any quantitative correlation between active Li loss due to interphasial changes and capacity fade in the cell. XPS, on the other hand, provides quantitative estimations of the SEI composition but is limited by its shallow penetration depth of only a few nanometers from the surface. Titration-based techniques, in this regard, have emerged as more precise quantitative tools for estimating Li loss due to SEI formation and dead Li accumulation.[26] Although each of these techniques has its own limitations, their combined application can complement one another and provide a comprehensive analysis. However, despite the utility of these techniques in characterizing the interphase of Li metal electrodes, their applicability is generally restricted to the initial few cycles. This restriction hinders their ability to provide information on the evolution of the interphase over prolonged cycling periods. Furthermore, given the fragility of Li metal electrodes under extended cycling, it is crucial to avoid any physical damage to the electrodes. This necessitates the introduction of noninvasive characterization techniques to ensure accurate and reliable analysis.

In this context, the characterization of the interphase using noninvasive techniques such as X-ray and neutron-based imaging techniques is highly beneficial.[18,42–51] These techniques offer several advantages: they do not damage the samples, can be employed both in situ and ex situ, closely resemble the actual cell configuration, and allow data acquisition over extended cycling periods. In this review, we discuss recent progress in non-destructive analytical methods for the characterization of high-energy-designed liquid electrolyte-based LMBs, focusing on their potential to enhance our understanding of interphasial dynamics and to drive the development of more robust high-energy-density batteries. Given the extensive number of review articles that discuss the application of various in situ and ex situ analytical techniques, this article specifically highlights the use of non-destructive methods in the study of LMBs.[34,52–54] Despite significant advancements in all-solid-state LMBs and the broad application of cutting-edge analytical techniques, the scope of this review is limited to liquid electrolyte-based LMBs. The primary rationale for this focus is the distinct degradation mechanisms between liquid electrolyte-based and solid-state LMBs. By focusing on LMBs with liquid electrolytes, this review aims to enhance the understanding of interphasial evolution at the Li electrode due to its complex interactions with liquid electrolytes and the subsequent impact on the stability and performance of LMBs.

2. Lithium Metal Degradation Mechanism Under High Energy Density Condition

In this section, let us clarify the importance of a series of technological parameters, such as the amount of electrolyte, areal capacity, and Li utilization ratio for realizing the cell-level high energy density rechargeable LMBs. The electrolyte-to-capacity ratio (E/C) is empirically utilized as a technological parameter for the cell design of LIB.[55] Even in the case of LMBs, the E/C plays a crucial role not only in cell-level energy density but also in cycle life. For example, Chen et al. explored the relationship between E/C and the cycle life of LMBs.[56] In their study, they used an NMC622 electrode with an areal capacity of 3.8 mAh cm^{-2} and a 250 μm thick Li metal foil as the positive and negative electrodes, respectively. As observed in Figure 1a, the LMB cell with an E/C of 25 g Ah^{-1} maintained stable capacity over 60 cycles before experiencing a sudden capacity drop. In stark contrast, an LMB cell with an E/C of 3 g Ah^{-1} showed a sudden capacity drop after only around 10 cycles. They also examined the relationship between E/C and cell-level energy density in LMBs using a relatively thin Li metal foil with a

Arghya Dutta is currently serving as a NIMS Special Researcher at the National Institute for Materials Science in Tsukuba, Japan. With over a decade of experience, he specializes in the research and development of electrochemical energy storage and conversion devices. His current research endeavors are centered around the mechanistic study, failure analysis, and electrolyte design aimed at enhancing the performance of lithium metal-based rechargeable batteries.

Shoichi Matsuda is a Team Leader at the National Institute for Materials Science (NIMS), Japan. He studied chemistry in The University of Tokyo and received his PhD in 2015. After that, he joined NIMS as an ICYS researcher and then got a tenured position in 2017. He was awarded the Young Researcher Award of The Electrochemical Society of Japan (2023), Young Scientists' Award by the Commendation for Science and Technology by the MEXT of Japan in 2024. His current research interests are high energy density rechargeable batteries and data-driven automated experiments.

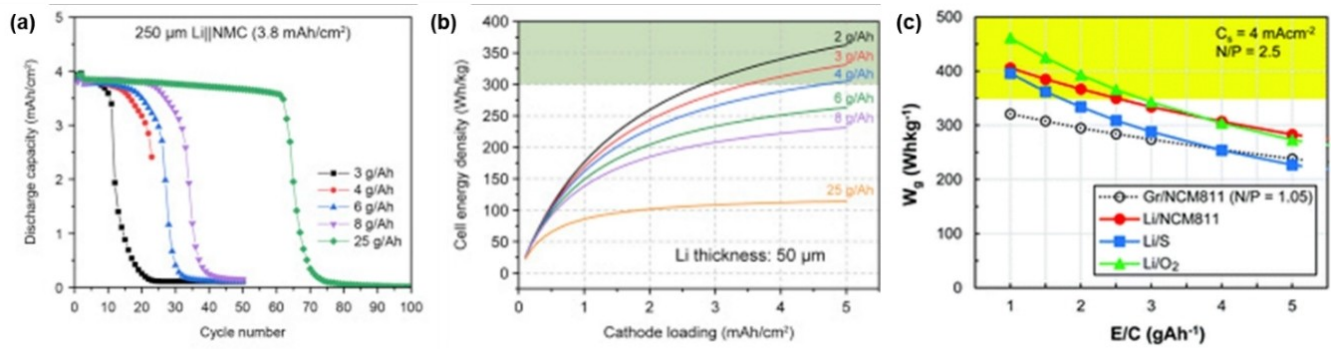

Figure 1. (a) Cycling stability of coin cells with NMC622 cathodes of 3.8 mAh cm^{-2}, 250 μm Li foil anodes, and various amounts of electrolyte. (b) Calculated energy densities of Li|NMC622 pouch cells with a 50 μm Li-metal anode and various cathode loadings and various electrolyte contents. Reproduced with permission from ref (56). Copyright 2019 Elsevier. (c) Calculated energy densities of 1 Ah pouch cells of different electrochemistry as a function of electrolyte amount (E/C). Reproduced with permission from ref (55). Copyright 2020 The Royal Society of Chemistry.

thickness of 50 μm. Figure 1b shows that with an E/C of 25 g Ah^{-1}, the cell-level energy density was less than 150 Wh kg^{-1}, despite the areal capacity being over 4 mA cm^{-2}. Conversely, with an E/C of 2 g Ah^{-1}, the energy density exceeded 300 Wh kg^{-1}. These results clearly demonstrated the significant impact of E/C on the cycle life and energy density of LMBs. It is also important to note that understanding the degradation mechanism of high-energy density LMBs accurately requires analyzing Li metal in an electrochemical cell environment designed with appropriate technological parameters. Similar investigations into the relationship between E/C and cell-level energy density have been conducted for other LMBs, such as lithium-sulfur (Li–S) and lithium-oxygen (LOB) batteries, yielding comparable conclusions (Figure 1c).[57] In particular, in LOB, several groups have reported high-energy density cells, and it is clear that there is a very good correlation between the cell level energy density and E/C.

In high energy density LMBs designed with a high-loading positive electrode, limited Li, and a lean electrolyte, the degradation of the Li metal electrode becomes complex.[58] The limited reservoir of Li and a small amount of electrolyte irreversibly react with each other, leading to consumption of both during each cycle. As a result, cell failure can occur due to a shortage of Li, electrolyte, or both. Niu et al. studied the failure mechanisms in a 1 Ah class LMB with a cell level specific energy of 300 Wh kg^{-1}, which is realized by a novel cell design featuring high mass loaded NMC622 positive electrode (3.8 mAh cm^{-2}), a thin metallic Li electrode (50 μm), and a limited electrolyte quantity (3 g Ah^{-1}).[20] The LMB cell containing 1.2 M lithium bis(fluorosulfonyl)imide (LiFSI) in a solvent mixture of triethyl phosphate and bis(2,2,2-trifluoroethyl) ether (TEP/BTFE, 1:2 molar ratio) demonstrated stable charge/discharge performance over 200 cycles, retaining 86% of its capacity. Although the initial thickness of the Li metal electrode was only 50 μm, it significantly increased to 120–160 μm after just 50 cycles and nearly 200 μm after 200 cycles (Figure 2a–c). Ex situ SEM analysis of the Li metal electrode showed considerable volume expansion and increased porosity of the electrode. Cross-sectional SEM revealed an expanded porous SEI layer on the electrode surface, with unused Li underneath, indicating that electrolyte depletion was the primary cause of cell failure. In high-energy pouch cells, the limited Li and electrolyte, combined with significant cell swelling, result in inadequate wetting of newly exposed Li surfaces during cycling. Ensuring proper wetting of these surfaces is essential for continuous electrochemical reactions.

The degree of cell swelling (Δt) was plotted against the cycle number (N) using logarithmic scales (Figure 2d). The parameters log (N) and log (Δt) were found to be linearly proportional with varying slopes, indicating two distinct regions of Li metal structural evolution. In region I (the initial 50 cycles), the flat Li foil transformed into solid large Li particles covered by SEI constituents, leading to rapid volume expansion of the Li metal electrode and quick cell thickening. Despite the formation of Li particles, a compatible electrolyte and uniform pressure helped slow down cell swelling and extended the cycle life. In region II (subsequent long-term cycling), the external pressure maintained optimal contact between individual Li particles, ensuring a percolation pathway for both ions and electrons. Additionally, it drove the lean electrolyte to wet newly formed Li surfaces, allowing electrochemical reactions to continue within the Li particles.

Matsuda et al. examined the structural changes of Li metal electrodes under low E/C conditions, where the areal capacity was 4 mAh cm^{-2} and the total electrolyte amount in the cell was 10 μL cm^{-2}.[58] They fabricated Li|Li symmetric cells and analyzed the structural changes of the electrodes using ex situ SEM equipped with energy dispersive spectroscopic (EDS) analysis (Figure 2e-h). For the cell with a 200 μm thick Li metal electrode, SEM images (Figure 2e, f) after the 10th Li deposition showed an increase in thickness to 220 μm. The electrode comprised three layers: (i) a 20 μm thick deposited Li layer, (ii) a 30 μm thick porous matrix layer composed of SEI and dead Li, and (iii) a 170 μm thick unreacted Li layer. In the case where a 20 μm thick Li foil was used as the electrode, the Li utilization ratio exceeded 90%. SEM analysis (Figure 2h) after the 10th Li deposition revealed that the electrode thickness reached approximately 90 μm, more than four times the initial Li foil thickness. Detailed examination showed the electrode consisted of three regions: (i) 5–10 μm sized metallic Li particles, (ii)

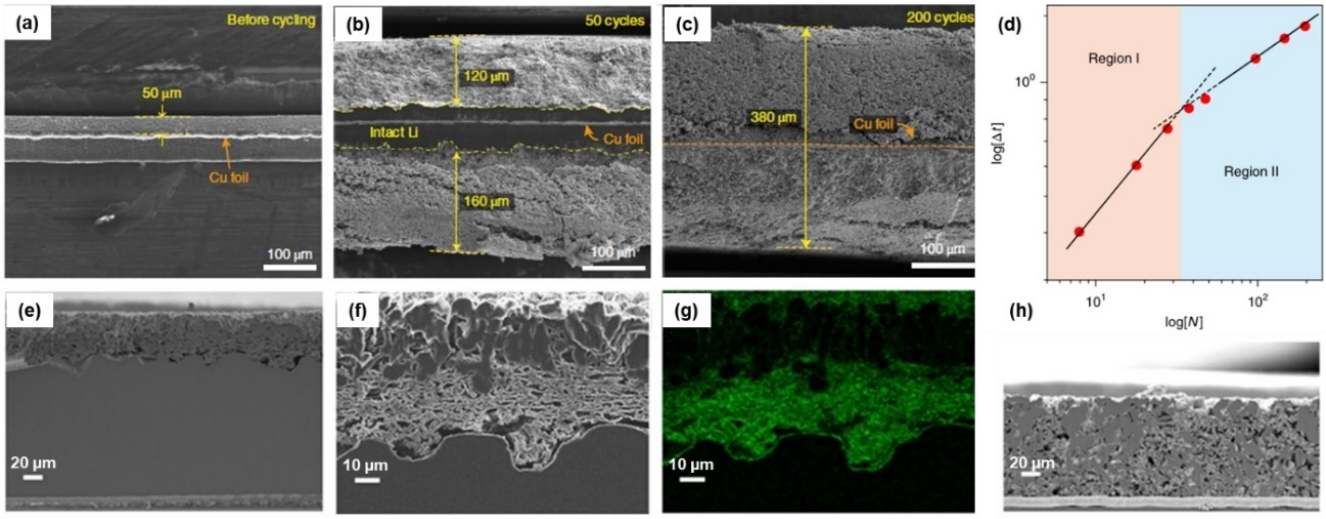

Figure 2. Cross-sectional SEM images of Li metal anodes consisting of Li foils on both sides of the Cu foil (8 μm thick) from Li||NMC622 pouch cells (3.8 mAh cm^{-2}) (a) before cycling, (b) after 50 cycles, and (c) after 200 cycles. (d) The degree of cell swelling plotted as a function of the cycle number using log scales. Reproduced with permission from ref (20). Copyright 2019 Springer Nature. (e,f) Cross-sectional SEM and (g) EDS image of a 200 μm thick Li electrode from a Li|Li symmetric cell after 10 cycles (4 mAh cm^{-2}). (h) Cross-sectional SEM image of a 20 μm thick Li electrode from a Li|Li symmetric cell after 10 cycles (4 mAh cm^{-2}). Reproduced with permission from ref (58). Copyright 2023 American Chemical Society.

aggregates measuring hundreds of nanometers, and (iii) micrometer-sized voids. These voids were filled with electrolytes during the Li dissolution/deposition reaction, facilitating Li-ion transport within the electrode.

In high-energy-density LMBs designed with suitable technological parameters, the significant volume expansion of Li metal electrodes is a key factor in determining cycle life. Most studies analyzing the structural changes in Li metal electrodes rely on ex situ SEM analysis. However, this method inevitably damages the electrodes during cell disassembly, cleaning, and drying processes, preventing a clear identification of their actual condition. Particularly for Li metal electrodes that have undergone repeated charge/discharge cycles under practical cell conditions, they become very fragile due to increased porosity, and their structure easily collapses when released from the cell constraints. Therefore, non-destructive analytical techniques are essential to accurately monitor and understand structural changes in Li metal electrodes. In the following sections, we will discuss the potential and recent advancements of X-ray and neutron-based imaging techniques for high energy density LMB analysis.

3. Application of X-Ray Imaging Technique in LMBs

X-ray computed tomography (XCT) is widely recognized in medical and scientific fields as a non-destructive imaging technique that derives contrast from the absorption coefficients of different materials. The X-ray beam, attenuated by its interaction with the sample, is collected and processed using advanced algorithms to generate cross-sectional and three-dimensional (3D) images. Since its initial application in 1971, laboratory-based XCT technology has seen significant advancements, particularly in achieving spatial resolutions at the nanometer scale.[59–61] As a result, XCT has proven to be an invaluable tool for evaluating batteries and related materials.[51] In particular, the use of synchrotron-based XCT with high-brilliance beamlines enables faster imaging and greater sensitivity compared to that of laboratory-based XCT. This translates to faster image acquisition, enhanced sensitivity, and the ability to achieve higher spatial and temporal resolutions. Such powerful synchrotron-based XCT offers several distinct advantages for the analysis of LMBs.

Sadd et al. utilized an operando synchrotron XCT (Figure 3a) to track the evolution of deposited Li metal and distinguish the formation of electrochemically inactive Li from the active bulk of Li microstructures.[49] The cell material was polyether ether ketone, which minimized X-ray attenuation while providing good sealing for the electrodes and electrolyte. Additionally, the middle section of the tube fitting was cut to reduce the outer diameter of the cell, and the electrodes were mounted. This novel electrochemical cell design, combined with a high flux synchrotron X-ray beam, enabled the fast acquisition of tomograms (63 seconds for a full tomogram) with enhanced contrast between Li and surrounding components. All tomograms were collected within a field of view of 0.8 mm and a voxel size of 0.325 μm, resulting in a spatial resolution of around 1 μm. For operando XCT measurement, a Li/Cu half-cell with 1.0 M Lithium bis(trifluoromethanesulfonyl)imide (LiTFSI) in 1,3-Dioxolane (DOL)/1,2-Dimethoxyethane (DME) was used, and the cell was cycled at 0.5 mA cm^{-2} (first cycle) and 1.0 mA cm^{-2} (second cycle). The reconstructed tomography (Figure 3b) showed that during the first cycle of plating at 0.5 mA cm^{-2}, needle-like microstructures were the primary form of deposited

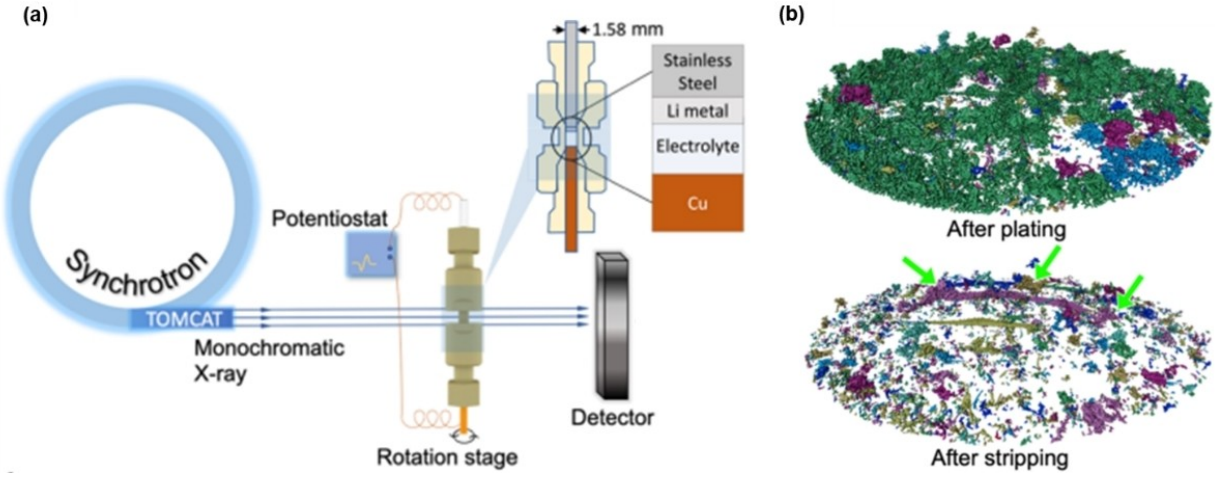

Figure 3. (a) Schematic illustration of the operando X-ray tomographic microscopy setup. (b) 3D renderings of segmented Li and identification of isolated regions, after plating and after stripping at 0.5 mA cm^{-2} for 1 h. Reproduced with permission from ref (49). Copyright 2023 Springer Nature.

Li, reaching heights up to 60 μm after 1 hour of plating. During the stripping process, some of these needle-like structures remained electrochemically active and nearly disappeared as stripping progressed. In contrast, some Li microstructures were only partially dissolved during stripping, with nearly half of the deposits remaining on the copper substrate at the end of the process, directly highlighting the formation of inactive Li. When the current density was increased to 1.0 mA cm^{-2} in the second cycle, rapid growth of a moss-like microstructure was observed. Another significant feature observed during plating at high current density was the growth of a large Li microstructure, which combined both mossy and needle-like morphologies and reached a height of 90 μm after 1 hour of plating. This type of Li microstructure is particularly hazardous due to its rapid vertical growth and the potential for small branches to penetrate a porous separator in the cell, leading to an internal short circuit.

Several groups have reported the structural analysis of Li metal electrodes using synchrotron-based XCT.[50] However, most of these studies used custom-made electrochemical cells designed to maximize spatial and temporal resolution, adapting to the limited beam time available at synchrotron facilities. Consequently, several key technological parameters are not well controlled from the perspective of practical LMB cell design. For instance, synchrotron-based XCT cells often contain excess electrolytes, thick glass fiber separators, and low areal capacity.[62] These factors significantly influence the degradation mechanism of Li electrodes and the cycle life of LMBs, as discussed in Section 2. Therefore, to accurately understand the degradation mechanism of Li metal electrodes, applying XCT techniques to high energy density LMBs is crucial. In the field of LIBs, many studies have explored synchrotron XCT applications for cylindrical and/or pouch-type LIBs. In contrast, the use of XCT techniques for analyzing LMBs with practical cell designs is limited, primarily due to the specific technical challenges involved in fabricating LMB cells. To our knowledge, the application of synchrotron XCT to LMBs with practically high energy density has not yet been reported. In contrast, several studies have used laboratory-based XCT for analyzing high energy density LMBs, although this method requires much longer measurement times to achieve a resolution comparable to synchrotron XCT.[18,19] Consequently, real-time operando measurements are not feasible with laboratory-based XCT. However, laboratory-based XCT offers the advantage of easier access to machine time, allowing for more flexible experiment designs. This is in contrast to synchrotron XCT, where access is limited by beamline availability and scheduling, necessitating careful planning and coordination.

Dutta et al. reported the application of laboratory-based XCT on 300 Wh kg^{-1} class LMBs (Figure 4a).[18] These LMBs were fabricated with high areal-capacity NMC811 positive electrodes (30 mg cm^{-2}, 6.6 mAh cm^{-2}), thin lithium metal negative electrodes (50 μm, 9.8 mAh cm^{-2}), and lean electrolyte conditions (10 μL cm^{-2}). As a result, the E/C was less than 2 g Ah^{-1}, meeting the requirements for high energy density LMBs, as described in Section 2. X-ray CT analyses of the pouch-type LMB cells were carried out with a source voltage and power of 140 kV and 10 W, respectively. The measurement time was approximately 12 hours, and the pixel resolution of the obtained images was 3.385 μm. The fabricated LMB cells were cycled at different discharge rate conditions. Notably, the cell cycled at a higher discharge current density (3 mA cm^{-2}) showed better cycle life than the one cycled at a lower discharge rate (0.6 mA cm^{-2}) (Figure 4b). To elucidate the detailed mechanism behind this discharge rate-dependent cycle life difference, XCT analysis was performed. Under low-rate discharge conditions, the initial thickness of the 50 μm Li-metal electrode increased to approximately 112 μm after 20 cycles of plating/stripping (Figure 4c). Conversely, under high-rate discharge conditions, the electrode thickness increased to 75 μm after 20 cycles (Figure 4d). These results clearly revealed that the thickness growth of the Li electrode is substantially suppressed when the cell is discharged at a relatively higher rate. The magnified cross-sectional XCT image and selected slice images (Figure 4e) of the

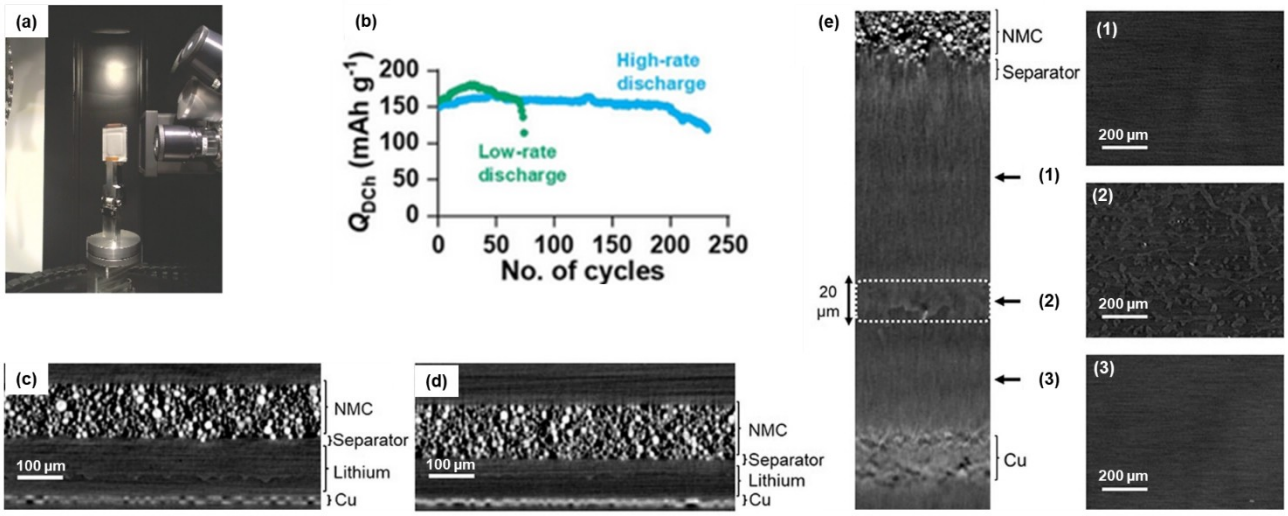

Figure 4. (a) Photographic image of XCT measurement set up. (b) Capacity vs. Cycle-life plot of a Li | NMC811 cell. Cross-sectional XCT images of pouch cell After 20th cycle at (c) low-rate discharge (0.6 mA cm^{-2}) and (d) high-rate discharge (3 mA cm^{-2}) under low-rate charge (0.6 mA cm^{-2}) conditions. (e) Magnified cross-section XCT images of pouch cell after 20th cycle at low-rate discharge. Reproduced with permission from ref (18). Copyright 2023 Wiley-VCH.

Li electrode from the low-rate discharged cell showed a three-layered structure in the Li metal electrode: (1) the top layer near the separator, (2) the middle layer, highlighted by a white dashed line, and (3) the bottom layer attached to the Cu foil. Considering the initial thickness of the Li metal electrode was 50 μm, the bottom layer could be identified as the unused metallic Li foil. The middle and top layers could be identified as composites of SEI compounds and dead Li. The slice XCT image revealed the formation of several tens of micrometer-sized particles in the middle layer, indicating that dead Li was the main component of this layer. In contrast, the XCT image of the top layer did not show a clear structure, suggesting that SEI compounds are the main component in this layer.

4. Application of Neutron Imaging Techniques in LMBs

Unlike X-rays, which primarily interact with the electron clouds of atoms, neutrons are uncharged particles that interact with atomic nuclei. This fundamental difference gives neutron-based imaging techniques several unique advantages. While X-ray attenuation is significantly affected by the atomic number, with heavier elements causing greater attenuation, neutron attenuation is largely independent of atomic number. As a result, neutron imaging (NI) is a highly effective tool for analyzing LMB components, owing to the high neutron sensitivity to low-Z materials, such as Li and hydrogen, which are difficult to visualize by X-ray-based imaging techniques (XIs).[63] Additionally, because the nucleus is much smaller than the electron cloud, neutrons are only weakly absorbed by many common materials. As a result, NI can effectively probe structures hidden within dense metallic environments. Another significant advantage of NI is its sensitivity to isotopes, which allows for isotopic labeling—a powerful technique where specific isotopes within battery components are selectively reported.

Although NI complements XI by excelling at visualizing materials and features that are challenging for X-rays, this advantage is counterbalanced by certain limitations. The interaction between neutrons and atomic nuclei is inherently weak, resulting in lower neutron fluxes compared to X-ray sources. Consequently, NI often experiences lower counts reaching the detector, leading to higher noise levels and lower signal-to-noise ratios in the images. This necessitates longer exposure times to achieve comparable image quality to XI. In terms of spatial resolution and temporal resolution, neutron-based analysis cannot compete with X-ray-based analysis simply from the viewpoint of structural analysis of metallic Li electrodes.

Song et al. demonstrated the use of time-resolved NI to study the dendrite growth of Li, a major cause of short circuits in Li-metal batteries, and the dynamic redistribution processes of Li during plating and stripping.[42] They used a custom-made cell (Figure 5a) with the cell body having an inner diameter of 10.6 mm, which fits the neutron beam size. To maximize the amount of deposited Li on the anode side, a $LiMn_2O_4$ positive electrode with high mass loading (thickness: 800 μm, capacity over 20 mAh cm^{-2}) was utilized. A deuterated electrolyte (d-ethylene carbonate and d-dimethyl carbonate containing $LiPF_6$ (1 M) in a 3 : 7 volume ratio) was used to reduce the incoherent scattering of hydrogen. In addition, to enhance the contrast between the Li metal deposits and the Li metal electrode, isotopic ^{7}Li was utilized, which has a higher attenuation coefficient than natural Li. The measurements were carried out using a polychromatic cold neutron beam with an intensity of 2.2×10^6 n cm^{-2} s^{-1} The 2D radiographic image with an effective resolution of approximately 100 μm could be obtained within a measurement time of 30 sec (Figure 5b). In comparison, it takes more than 10 hours to obtain a 3D tomographic image. The 3D

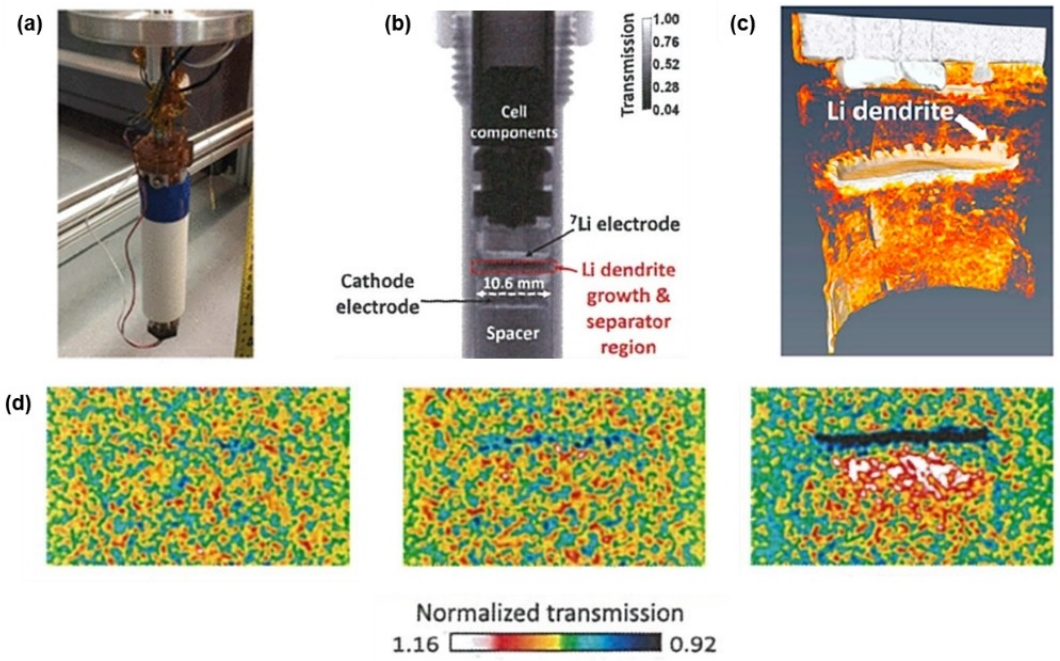

Figure 5. (a) Photographic image of the netron imaging cell. (b) 2D radiographic image after 30 sec and C) 3D tomographic image after 12 h. (d) 2D evolution of Li distribution with different charging time. Reproduced with permission from ref (42). Copyright 2019 American Chemical Society.

tomographic image after the cell charged for 30 hours, at which the estimated amount of deposited Li metal was 80 μm, is shown in Figure 5c. The white/yellow regions in the positive electrode/separator represent the distribution and morphology of natural Li in the form of $LiMn_2O_4$ particles and $LiPF_6$ salt in the electrolyte. The ^{7}Li metal electrode remains invisible due to its low neutron absorption cross-section. Notably, the dendritic formation of deposited Li metal was clearly observed, revealing the effectiveness of NI techniques for structural analysis of Li electrodes. Although 3D tomographic image provides visualization evidence of dendrite growth and Li distribution, the dynamic features could only be revealed by real-time 2D radiography during battery operation. Figure 5d shows time-resolved in situ neutron radiography during the charging process. Due to the high neutron attenuation coefficient of Li, regions with high Li concentration show strong attenuation of the incident neutron beams, resulting in reduced transmitted intensity through these areas. Conversely, regions with low Li concentration exhibit weak attenuation, leading to increased transmitted intensity. As a result, the transmitted intensity through the high Li concentration region appeared dark, colored by a dark blue region. In contrast, the region with low Li concentration appeared bright, which is colored by red/white regions. With the progress of the charging reaction, there can be seen the deposition of Li metal deposits at the separator/Li metal electrode interface, which is colored as blue regions. In addition, the depletion of Li from the positive electrode region is also observed in the form of the appearance of red/white regions.

Ziesche et al. reported the application of neutron topographic analysis of commercial CR2-type primary LMB with a height of 27 mm and width of 15.6 mm diameter (Figure 6a).[43] The cell consisted of an MnO_2 positive electrode and a Li metal negative electrode supplied by Duracell. The tomographic NI was carried out using a polychromatic cold neutron beam with a neutron flux of 2.7×10^6 n cm^{-2} s. A camera with 2048×2048 pixels was utilized, resulting in a pixel size of 12.9 μm. The discharge process was interrupted during tomography acquisition due to the long exposure time of 8 h per tomogram. Figure 6b revealed the orthogonal slices of the neutron tomogram, where the Li electrode and the excess electrolyte in the middle of the cell are clearly visible. With the progress of the discharge process, there can be seen the inhomogeneity of Li removal from the Li metal electrode (blue arrow in Figure 6b). In addition, Inhomogeneous electrolyte consumption is also observed as shown in the yellow arrow. Figure 6c shows the vertical cross-sectional neutron tomographic image obtained during the discharge process with different SOC. With the progress of the discharge process, there can be clearly seen a decrease in electrolyte stored in the middle part of the cell. It should be noted that during the discharging process the excess electrolyte, which is mainly stored in the middle core of the cell, is consumed where a part may be used for forming an excess amount of SEI. The excess electrolyte helps to compensate for the electrolyte consumption and maintain the Li-ion conductivity between the electrodes during operation. During discharging, the excess electrolyte is consumed steadily and disappears from the inner region of the cell.

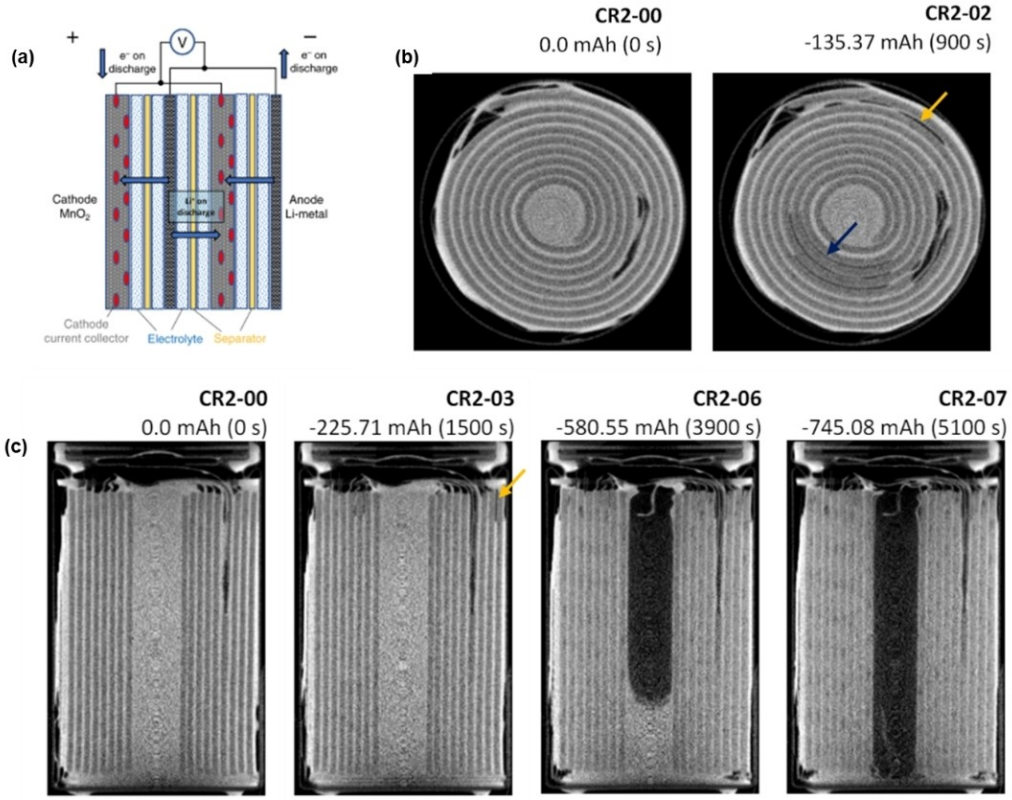

Figure 6. (a) An illustration of the studied Li/MnO_2 CR2 primary cell from Duracell. (b) Horizontal and (c) vertical slices of neutron tomograms. Reproduced with permission from ref (43). Copyright 2020 Springer Nature.

5. Summary and Outlook

In this review article, we overview the applications of non-invasive characterization techniques used to study the degradation of LMBs. These techniques aim to address key issues such as the morphological evolution of Li metal, interphase growth, and quantitative assessment of cell degradation without causing physical damage to cell components. Non-invasive tools have successfully captured the microstructures of Li, revealing the heterogeneous growth of Li metal in three dimensions. Both laboratory-based and synchrotron XCT techniques have provided detailed insights into complicated structural changes of Li electrodes. These observations help us understand Li growth behaviors and interphase formation, which are crucial for identifying the root causes of cell failure, such as Li depletion or electrolyte consumption. However, lab-based XCT suffers from low resolution, while synchrotron XCT, though resolving this issue, faces the challenge of limited beamtime availability in many cases. Moreover, XCT techniques struggle with detecting low atomic number elements. NI is a highly effective tool for analyzing the degradation mechanism of LMB, owing to the high neutron sensitivity of low-Z materials, such as Li and hydrogen. Although the NI technique requires longer measurement time compared to the XI technique. NI can provide complements of XI by excelling at visualizing materials and features that are challenging for X-rays, such as concentration change of Li ions and movement of the electrolyte. Despite the promising potential of Li metal electrodes, practical LMBs face several challenges, including an insufficient understanding of degradation mechanisms. Recent advancements in state-of-the-art techniques have shed light on some of these mechanisms. Each technique has its limitations, but collectively, they have significantly enriched our understanding of Li metal electrodes. To develop high-energy-density LMBs, focusing on non-invasive characterization techniques using practical cell configurations is essential. Complementary use of multiple tools can provide a more comprehensive understanding of cell processes, overcoming individual technical limitations.

Conflict of Interests

The authors declare no conflict of interest.

Keywords: Battery analysis · Noninvasive techniques · XCT · Neutron imaging · Li-metal electrode

[1] M. Armand, J.-M. Tarascon, *Nature* **2008**, *451*, 652.
[2] J. W. Choi, D. Aurbach, *Nat. Rev. Mater.* **2016**, *1*, 16013.
[3] X. Shen, H. Liu, X.-B. Cheng, C. Yan, J.-Q. Huang, *Energy Storage Mater.* **2018**, *12*, 161.
[4] D. Lin, Y. Liu, Y. Cui, *Nat. Nanotechnol.* **2017**, *12*, 194.
[5] X. Zhang, A. Wang, X. Liu, J. Luo, *Acc. Chem. Res.* **2019**, *52*, 3223.
[6] X. Gao, Y.-N. Zhou, D. Han, J. Zhou, D. Zhou, W. Tang, J. B. Goodenough, *Joule* **2020**, *4*, 1864.

[7] G. M. Hobold, J. Lopez, R. Guo, N. Minafra, A. Banerjee, Y. Shirley Meng, Y. Shao-Horn, B. M. Gallant, *Nat. Energy* **2021**, *6*, 951.
[8] R. Gu, D. Zhang, S. Zhu, J. Xu, K. Ding, Q. Gao, Q. Xu, P. Shi, H. Li, Y. Min, *Adv. Funct. Mater.* **2024**, *34*, 2310747.
[9] H. Su, Z. Chen, M. Li, P. Bai, Y. Li, X. Ji, Z. Liu, J. Sun, J. Ding, M. Yang, X. Yao, C. Mao, Y. Xu, *Adv. Mater.* **2023**, *35*, 2301171.
[10] K. Shi, A. Dutta, Y. Hao, M. Zhu, L. He, Y. Pan, X. Xin, L.-F. Huang, X. Yao, J. Wu, *Adv. Funct. Mater.* **2022**, *32*, 2203652.
[11] X. Xin, K. Ito, A. Dutta, Y. Kubo, *Angew. Chem. Int. Ed.* **2018**, *57*, 13206.
[12] J. Qian, W. A. Henderson, W. Xu, P. Bhattacharya, M. Engelhard, O. Borodin, J.-G. Zhang, *Nat. Commun.* **2015**, *6*, 6362.
[13] H. Wu, H. Jia, C. Wang, J.-G. Zhang, W. Xu, *Adv. Energy Mater.* **2021**, *11*, 2003092.
[14] X.-B. Cheng, R. Zhang, C.-Z. Zhao, F. Wei, J.-G. Zhang, Q. Zhang, *Adv. Sci.* **2016**, *3*, 1500213.
[15] X. Shen, R. Zhang, X. Chen, X.-B. Cheng, X. Li, Q. Zhang, *Adv. Energy Mater.* **2020**, *10*, 1903645.
[16] X.-R. Chen, C. Yan, J.-F. Ding, H.-J. Peng, Q. Zhang, *J. Energy Chem.* **2021**, *62*, 289.
[17] Y. Jiang, F. Ye, *Chem. Eur. J.* **2024**, *30*, e202400424.
[18] A. Dutta, E. Mizuki, S. Matsuda, *Batter. Supercaps* **2023**, *6*, e202300309.
[19] A. Dutta, E. Mizuki, Y. Tomori, S. Matsuda, *ACS Appl. Energy Mater.* **2024**, *7*, 3824.
[20] C. Niu, H. Lee, S. Chen, Q. Li, J. Du, W. Xu, J.-G. Zhang, M. S. Whittingham, J. Xiao, J. Liu, *Nat. Energy* **2019**, *4*, 551.
[21] D. Lu, Y. Shao, T. Lozano, W. D. Bennett, G. L. Graff, B. Polzin, J. Zhang, M. H. Engelhard, N. T. Saenz, W. A. Henderson, P. Bhattacharya, J. Liu, J. Xiao, *Adv. Energy Mater.* **2015**, *5*, 1400993.
[22] R. Lin, Y. He, C. Wang, P. Zou, E. Hu, X.-Q. Yang, K. Xu, H. L. Xin, *Nat. Nanotechnol.* **2022**, *17*, 768.
[23] J. Wang, W. Huang, A. Pei, Y. Li, F. Shi, X. Yu, Y. Cui, *Nat. Energy* **2019**, *4*, 664.
[24] A. Dutta, Y. Kubo, A. Nagataki, K. Matsushita, *ACS Appl. Mater. Interfaces* **2023**, *15*, 15467.
[25] R. Grissa, V. Fernandez, N. Fairley, J. Hamon, N. Stephant, J. Rolland, R. Bouchet, M. Lecuyer, M. Deschamps, D. Guyomard, P. Moreau, *ACS Appl. Energy Mater.* **2018**, *1*, 5694.
[26] C. Fang, J. Li, M. Zhang, Y. Zhang, F. Yang, J. Z. Lee, M.-H. Lee, J. Alvarado, M. A. Schroeder, Y. Yang, B. Lu, N. Williams, M. Ceja, L. Yang, M. Cai, J. Gu, K. Xu, X. Wang, Y. S. Meng, *Nature* **2019**, *572*, 511.
[27] G. M. Hobold, B. M. Gallant, *ACS Energy Lett.* **2022**, *7*, 3458.
[28] Y. Xiang, M. Tao, G. Zhong, Z. Liang, G. Zheng, X. Huang, X. Liu, Y. Jin, N. Xu, M. Armand, J.-G. Zhang, K. Xu, R. Fu, Y. Yang, *Sci. Adv.* **2024**, *7*, eabj3423.
[29] A. Dutta, K. Matsushita, Y. Kubo, *Adv. Sci.* **2024**, *11*, 2404245.
[30] B. Han, Z. Zhang, Y. Zou, K. Xu, G. Xu, H. Wang, H. Meng, Y. Deng, J. Li, M. Gu, *Adv. Mater.* **2021**, *33*, 2100404.
[31] K. N. Wood, G. Teeter, *ACS Appl. Energy Mater.* **2018**, *1*, 4493.
[32] M. Nagao, A. Hayashi, M. Tatsumisago, T. Kanetsuku, T. Tsuda, S. Kuwabata, *Phys. Chem. Chem. Phys.* **2013**, *15*, 18600.
[33] M. Golozar, A. Paolella, H. Demers, S. Bessette, M. Lagacé, P. Bouchard, A. Guerfi, R. Gauvin, K. Zaghib, *Commun. Chem.* **2019**, *2*, 131.
[34] Z. Zhang, S. Said, K. Smith, R. Jervis, C. A. Howard, P. R. Shearing, D. J. L. Brett, T. S. Miller, *Adv. Energy Mater.* **2021**, *11*, 2101518.
[35] B. Wolff, F. Hausen, *J. Electrochem. Soc.* **2023**, *170*, 010534.
[36] M. Golozar, P. Hovington, A. Paolella, S. Bessette, M. Lagacé, P. Bouchard, H. Demers, R. Gauvin, K. Zaghib, *Nano Lett.* **2018**, *18*, 7583.
[37] Q. Li, T. Yi, X. Wang, H. Pan, B. Quan, T. Liang, X. Guo, X. Yu, H. Wang, X. Huang, L. Chen, H. Li, *Nano Energy* **2019**, *63*, 103895.
[38] L. Zhang, T. Yang, C. Du, Q. Liu, Y. Tang, J. Zhao, B. Wang, T. Chen, Y. Sun, P. Jia, H. Li, L. Geng, J. Chen, H. Ye, Z. Wang, Y. Li, H. Sun, X. Li, Q. Dai, Y. Tang, Q. Peng, T. Shen, S. Zhang, T. Zhu, J. Huang, *Nat. Nanotechnol.* **2020**, *15*, 94.
[39] H. Sun, Q. Liu, J. Chen, Y. Li, H. Ye, J. Zhao, L. Geng, Q. Dai, T. Yang, H. Li, Z. Wang, L. Zhang, Y. Tang, J. Huang, *ACS Nano* **2021**, *15*, 19070.
[40] P. Bai, J. Li, F. R. Brushett, M. Z. Bazant, *Energy Environ. Sci.* **2016**, *9*, 3221.
[41] J. Steiger, D. Kramer, R. Mönig, *J. Power Sources* **2014**, *261*, 112.
[42] B. Song, I. Dhiman, J. C. Carothers, G. M. Veith, J. Liu, H. Z. Bilheux, A. Huq, *ACS Energy Lett.* **2019**, *4*, 2402.
[43] R. F. Ziesche, T. Arlt, D. P. Finegan, T. M. M. Heenan, A. Tengattini, D. Baum, N. Kardjilov, H. Markötter, I. Manke, W. Kockelmann, D. J. L. Brett, P. R. Shearing, *Nat. Commun.* **2020**, *11*, 777.
[44] B. Song, G. M. Veith, J. Park, M. Yoon, P. S. Whitfield, M. J. Kirkham, J. Liu, A. Huq, *Chem. Mater.* **2019**, *31*, 124.
[45] R. F. Ziesche, N. Kardjilov, W. Kockelmann, D. J. L. Brett, P. R. Shearing, *Joule* **2022**, *6*, 35.
[46] F. Sun, D. Zhou, X. He, M. Osenberg, K. Dong, L. Chen, S. Mei, A. Hilger, H. Markötter, Y. Lu, S. Dong, S. Marathe, C. Rau, X. Hou, J. Li, M. C. Stan, M. Winter, R. Dominko, I. Manke, *ACS Energy Lett.* **2020**, *5*, 152.
[47] F. Sun, R. Moroni, K. Dong, H. Markötter, D. Zhou, A. Hilger, L. Zielke, R. Zengerle, S. Thiele, J. Banhart, I. Manke, *ACS Energy Lett.* **2017**, *2*, 94.
[48] K. R. Adair, M. N. Banis, Y. Zhao, T. Bond, R. Li, X. Sun, *Adv. Mater.* **2020**, *32*, 2002550.
[49] M. Sadd, S. Xiong, J. R. Bowen, F. Marone, A. Matic, *Nat. Commun.* **2023**, *14*, 854.
[50] F. Tang, Z. Wu, C. Yang, M. Osenberg, A. Hilger, K. Dong, H. Markötter, I. Manke, F. Sun, L. Chen, G. Cui, *Small Methods* **2021**, *5*, 2100557.
[51] J. Scharf, M. Chouchane, D. P. Finegan, B. Lu, C. Redquest, M. Kim, W. Yao, A. A. Franco, D. Gostovic, Z. Liu, M. Riccio, F. Zelenka, J.-M. Doux, Y. S. Meng, *Nat. Nanotechnol.* **2022**, *17*, 446.
[52] D. Liu, Z. Shadike, R. Lin, K. Qian, H. Li, K. Li, S. Wang, Q. Yu, M. Liu, S. Ganapathy, X. Qin, Q.-H. Yang, M. Wagemaker, F. Kang, X.-Q. Yang, B. Li, *Adv. Mater.* **2019**, *31*, 1806620.
[53] X. Liu, Z. Liang, Y. Xiang, M. Lin, Q. Li, Z. Liu, G. Zhong, R. Fu, Y. Yang, *Adv. Mater.* **2021**, *33*, 2005878.
[54] H. Park, O. Tamwattana, J. Kim, S. Buakeaw, R. Hongtong, B. Kim, P. Khomein, G. Liu, N. Meethong, K. Kang, *Adv. Energy Mater.* **2021**, *11*, 2003039.
[55] M. Ue, K. Sakaushi, K. Uosaki, *Mater. Horiz.* **2020**, *7*, 1937.
[56] S. Chen, C. Niu, H. Lee, Q. Li, L. Yu, W. Xu, J.-G. Zhang, E. J. Dufek, M. S. Whittingham, S. Meng, J. Xiao, J. Liu, *Joule* **2019**, *3*, 1094.
[57] S. Matsuda, M. Ono, S. Yamaguchi, K. Uosaki, *Mater. Horiz.* **2022**, *9*, 856.
[58] S. Matsuda, M. Ono, A. Myojin, *ACS Appl. Energy Mater.* **2023**, *6*, 2524.
[59] G. Di Chiro, R. A. Brooks, *J. Comput. Assist. Tomogr.* **1980**, *4*, 241.
[60] E. C. Beckmann, *Br. J. Radiol.* **2006**, *79*, 5.
[61] G. N. Hounsfield, *Br. J. Radiol.* **1973**, *46*, 1016.
[62] F. Sun, R. Gao, D. Zhou, M. Osenberg, K. Dong, N. Kardjilov, A. Hilger, H. Markötter, P. M. Bieker, X. Liu, I. Manke, *ACS Energy Lett.* **2019**, *4*, 306.
[63] R. F. Ziesche, N. Kardjilov, W. Kockelmann, D. J. L. Brett, P. R. Shearing, *Joule* **2022**, *6*, 35.

Manuscript received: July 26, 2024
Revised manuscript received: October 2, 2024
Accepted manuscript online: October 9, 2024
Version of record online: November 9, 2024